Junkai Lu[1]
Department of Mechanical Engineering,
University of California,
Berkeley, CA 94720
e-mail: junkai.lu@berkeley.edu

Kevin Haninger
Department of Mechanical Engineering,
University of California,
Berkeley, CA 94720
e-mail: khaninger@berkeley.edu

Wenjie Chen
FANUC Corporation,
Oshino-mura, Yamanashi
Prefecture 401-0597, Japan
e-mail: wjchen@berkeley.edu

Suraj Gowda
Department of Electrical Engineering
and Computer Sciences,
University of California,
Berkeley, CA 94720
e-mail: surajgowda@berkeley.edu

Masayoshi Tomizuka
Department of Mechanical Engineering,
University of California,
Berkeley, CA 94720
e-mail: tomizuka@me.berkeley.edu

Jose M. Carmena
Department of Electrical Engineering
and Computer Sciences,
Helen Wills Neuroscience Institute,
University of California,
Berkeley, CA 94720
e-mail: jcarmena@berkeley.edu

Design of a Passive Upper Limb Exoskeleton for Macaque Monkeys

Integrating an exoskeleton as the external apparatus for a brain–machine interface (BMI) has the advantage of providing multiple contact points to determine body segment postures and allowing control to and feedback from each joint. When using macaques as subjects to study the neural control of movement, an upper limb exoskeleton design with unlikely singularity is required to guarantee safe and accurate tracking of joint angles over all possible range of motion (ROM). Additionally, the compactness of the design is of more importance considering macaques have significantly smaller body dimensions than humans. This paper proposes a six degree-of-freedom (DOF) passive upper limb exoskeleton with 4DOFs at the shoulder complex. System kinematic analysis is investigated in terms of its singularity and manipulability. A real-time data acquisition system is set up, and system kinematic calibration is conducted. The effectiveness of the proposed exoskeleton system is finally demonstrated by a pilot animal test in the scenario of a reach and grasp task. [DOI: 10.1115/1.4033837]

1 Introduction

Brain–machine interfaces can provide means to enable communication between the brain and the outside world [1]. They are often aimed at assisting, augmenting, or repairing human cognitive or sensory-motor functions, especially for paralyzed patients. Researchers have used BMIs to allow able-bodied monkeys [2] and humans who suffer from brainstem stroke [3] to control robotic arms in three-dimensional (3D) reach and grasp tasks, which have helped promote a new paradigm of human–robot interaction.

On the other hand, traditional human–robot interaction is well established in the rehabilitation field. Particularly for upper limb rehabilitation, most existing therapy robots are either end-effector–based or exoskeleton devices [4]. Since an end-effector–based robot generally interacts with patients through only one point, it cannot fully determine the arm posture and the interaction torques at each joint. Although a wearable exoskeleton has a more complicated mechanical structure and system dynamics, the multiple contact points with the subject's body allow control to and feedback from each joint individually. An exoskeleton may more effectively restore the patient's mobility with control of the impaired limbs shared between the exoskeleton controller and the patient's residual motor control abilities.

Per the above discussions, an exoskeleton as an apparatus controlled by the BMI may more closely match natural motion, which may allow better study of the neural control of movement. Currently, most BMI researches are conducted with rhesus macaques (*Macaca mulatta*) as the study subjects, and the KINARM introduced in Ref. [5] is the only upper limb exoskeleton designed for nonhuman primates. It is a 2DOF actuated device allowing for movements in a two-dimensional plane. Most of the existing upper limb exoskeletons for 3D workspaces are dedicated to human rehabilitation, and their target functions and design requirements are different from what we would like to achieve. However, they can still serve as pilot examples to investigate.

Kinematic design is one of the key aspects for developing an upper limb exoskeleton, and matching a mechanical exoskeleton to a biological structure faces difficulties, especially in the shoulder complex. Specifically, two major problems are axis alignment between the anatomical and device joints and the kinematic singularity of mechanical models. The former problem arises with the fact that the shoulder center of rotation changes as a function of posture [6]. This can be explained by Fig. 1, which shows that the shoulder complex is a highly coupled mechanism of great complexity. It consists of four joints, and each joint possesses multi-DOFs [8]. A large amount of research has been conducted to reduce joint axis misalignment to guarantee the user's

[1]Corresponding author.

Contributed by the Dynamic Systems Division of ASME for publication in the Journal of Dynamic Systems, Measurement, and Control. Manuscript received December 6, 2015; final manuscript received April 27, 2016; published online July 27, 2016. Assoc. Editor: Hashem Ashrafiuon.

Copyright © 2016 by ASME

Downloaded From: http://dynamicsystems.asmedigitalcollection.asme.org/ on 05/14/2018 Terms of Use: http://www.asme.org/about-asme/terms-of-use

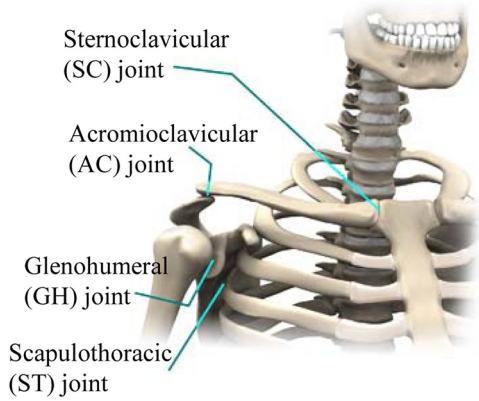

Fig. 1 Joints located at the shoulder complex [7]

ROM and comfort [4,9,10]. The other kinematic design difficulty is how to avoid the mechanical shoulder joint's singularity. A *kinematic singularity* refers to a configuration in which there is a change in the number of instantaneous DOFs, and the mechanism cannot move arbitrarily. This is highly undesirable for a motion tracking system. In the vicinity of a singularity for a motorized design, small desired velocities in the task space will require very large joint motions if the task space velocities have components along the degenerated directions. These large joint motions may damage the motors or even result in severe injuries to the user. Apart from the translational DOFs, the shoulder complex can be basically modeled by a ball-and-socket joint consisting of three rotational DOFs, which can be mechanically implemented using three serial revolute joints. The two conventions shown in Fig. 2 are widely used to describe the rotation sequence [11]. However, since both conventions use a triad model, singularities cannot be avoided if their postures require an alignment of their first joint axis with the third.

Compared with the axis alignment problem, the singularity issue in the shoulder complex design has not drawn the same amount of attention since rehabilitation-oriented exoskeletons typically do not require large ROM, and the training motions for patients are expected to be within certain patterns. Thus, mechanism singularities can be intentionally avoided. However, for an exoskeleton designed for macaques, when operated in the passive tracking mode where the macaque's arm is free to do arbitrary motion, a shoulder joint design with unlikely singularity is of significance for allowing precise tracking and addressing safety concerns, considering macaques are generally noncooperative. To reduce the occurrence of kinematic singularities, several research groups revised the aforementioned standard triad models based on different concerns and assumptions. Typical designs are (CADEN)-7 [12], MEDARM [9], and SAM [13]. (CADEN)-7 used a strategy of assigning the mechanism's singularity to a direction that is anthropometrically hard to reach in human's activities of daily living (ADL). In this way, it was claimed that the majority of the exoskeleton workspace is free of singularities. MEDARM utilized an optimization-based approach to define the relative angle between its first joint axis and the second. Using the proposed parameters, it was claimed that there is no singularity in their prescribed workspace. SAM is an intermediate design between (CADEN)-7 and MEDARM considering its first joint axis configuration as well as using the condition number of the Jacobian matrix (isotropic index) to evaluate system manipulability. However, all these designs used a triad joint model to mimic the shoulder complex, making each task space posture correspond to a unique inverse solution for the joint space realization; therefore, a singularity always exists.

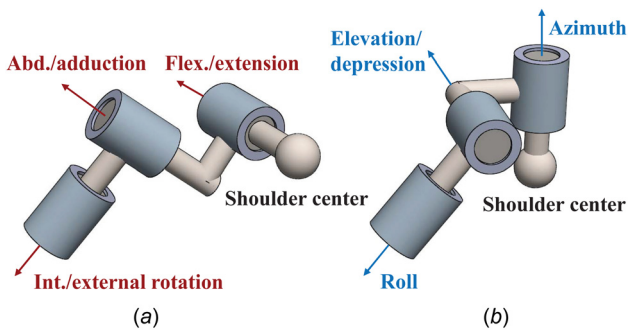

Fig. 2 Two rotation conventions for the glenohumeral joint model: (*a*) flexion–abduction–rotation and (*b*) azimuth–elevation–roll

This paper proposes a 6DOF upper limb exoskeleton model with 4DOFs at the shoulder complex to achieve better manipulability than conventional shoulder models. A nonmotorized prototype is built as a kinematic motion sensing device for offline neural decoding studies as well as for animal training purposes. In the first stage, passive kinematic motion data acquisition should be investigated to directly characterize the subject motion of each local joint (e.g., ROM and joint speed limit), which can provide guidance to the actuation system design for the next-generation actuated exoskeleton development. An entirely passive training apparatus is also safe to operate for the animal subjects which have not ever been exposed to an exoskeletonlike wearable robot. The exoskeleton should also be compact considering the macaques' small dimensions [14]. However, allowing better alignment between the mechanical and biological joints typically requires more DOFs, which will reduce the compactness of the mechanism design. To maintain a feasible design which can capture arbitrary motion, the kinematic singularity issue of the shoulder model is considered with priority here.

This paper is organized as follows: the exoskeleton system design is described in Sec. 2 including proposed modeling, mechanical design, and real-time data acquisition; kinematic analysis of the proposed shoulder joint model is conducted in Sec. 3 by investigating the model's joint limits, singularity, and manipulability; system kinematic calibration is conducted in Sec. 4 with the help of an external motion capture system; animal test results are finally presented in Sec. 5; and Sec. 6 concludes the paper.

2 Exoskeleton System Design

The designed BMI task for macaques is shown in Fig. 3. A macaque is seated in a primate chair with its collar and torso constrained, and the proposed exoskeleton is attached to the macaque's right upper limb for passively following and recording the voluntary motion of the arm to reach and grasp targets in the 3D presenting system. Meanwhile, the neural signal will also be recorded and synchronized with the motion data at the BMI host personal computer (PC).

2.1 Design Requirements. As previously discussed, for an exoskeleton model, a shoulder joint design with unlikely singularity is required for both large joint ROM and safety considerations. Although the safety issue is not as critical in a fully passive mechanism, it will be one of the major concerns in the control of a future motorized design.

The compactness is also of importance to an upper limb exoskeleton designed for macaques. Table 1 lists the key body dimensions of our BMI macaques in comparison to those of humans, which suggests that the space around the macaque upper limb is quite limited. Thus, the mechanical components of the exoskeleton should be kept sufficiently compact, and some complicated designs good for adult humans may not be applicable to macaques with relatively smaller body dimensions.

Human physiological and ADL ROMs are referenced (in the third and the fourth columns of Table 2, averaged from Refs. [10],

Downloaded From: http://dynamicsystems.asmedigitalcollection.asme.org/ on 05/14/2018 Terms of Use: http://www.asme.org/about-asme/terms-of-use

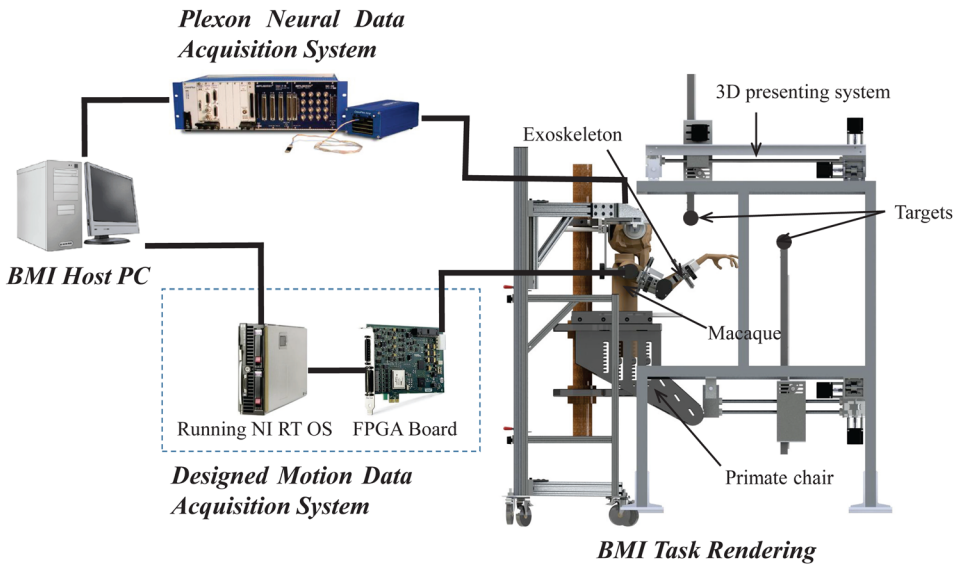

Fig. 3 Overview of the designed 3D BMI task for a macaque subject

Table 1 Key upper limb dimensions comparing BMI macaques versus humans

	Length (cm)		Circumference (cm)	
Subjects	Upper arm	Forearm[a]	Upper arm	Forearm
Macaque G	14.5	15.2	23.2	16.2
Macaque J	13.7	16.2	24.5	18.0
Macaque W	14.2	16.3	23.5	17.1
Human	37.4[b]	48.8[b]	31.8[c]	24.2[c]

[a]From elbow to hand.
[b]Average of male and female data from Ref. [15].
[c]Data from Ref. [16].

[12], and [17]), which are sufficient to cover the workspace (in front of the coronal plane of macaque body) in the proposed BMI tasks. Additionally, it is assumed that the elevation/depression and protraction/retraction of the macaque shoulder are negligible during BMI task motions.

2.2 Mechanical Models of Upper Limb Joints. The functionality of primate upper limbs is determined by the shoulder complex, elbow complex, wrist, and hand.

The shoulder complex is one of the most difficult structures to model for an upper limb. Although Christel and Billard [18] and Chan and Moran [19] point out that the morphology of the macaque shoulder joint is not exactly the same as a human's, human upper limb structure can still serve as a reference for developing the kinematic design of an exoskeleton in the absence of macaque shoulder joint models in existing literature. A nonredundant 5DOF mathematical model of the shoulder complex for humans is proposed in Ref. [20] including three rotational DOFs (abduction/adduction, flexion/extension, and internal/external rotation) and two translational DOFs (elevation/depression and protraction/retraction) with the thorax as the fixed base. However, in the engineering world, for simplicity, mostly only the glenohumeral joint (Fig. 1) is modeled for the shoulder complex using a ball-and-socket joint model, as shown in Fig. 4(*a*). The elbow complex mainly consists of the elbow joint and the radioulnar joint. The former is commonly modeled using a hinge joint as shown in Fig. 4(*b*), and the latter is generally regarded as a pivot joint corresponding to pronosupination of the forearm as shown in Fig. 4(*c*). This DOF can be included either with the elbow or with the wrist, and serves as a revolute joint connecting the elbow and the wrist.

Considering the upper limb motion of interest in the BMI study, the wrist and the hand motions and their modeling are not investigated in this paper.

Table 2 Human ROM and the designed mechanical limits

Joint	Motion	Phy. ROM (deg)	ADL ROM (deg)	Mech. limit (deg)
1	Azi. add./abd.	—	170	191.0
2	Shld. add./abd.	182	145	276.6
3	Shld. flx./ext.	249	110	196.2
4	Shld. int./ext.	187	150	160.0
5	Elbw. int./ext	142	140	96.8
6	Pron./supi.	190	135	160.0

2.3 Mechanical Design. Kinematically redundant mechanisms enjoy flexibility in positioning and tracking due to their possession of more DOFs than required. Accordingly, a 6DOF upper limb exoskeleton design is proposed in Fig. 5. Four DOFs are assigned to the shoulder complex by integrating the azimuthal rotation joint from convention Fig. 2(*b*) to the whole triad model in convention Fig. 2(*a*). With an extra DOF at the shoulder joint, better mechanism manipulating ability can be achieved. The

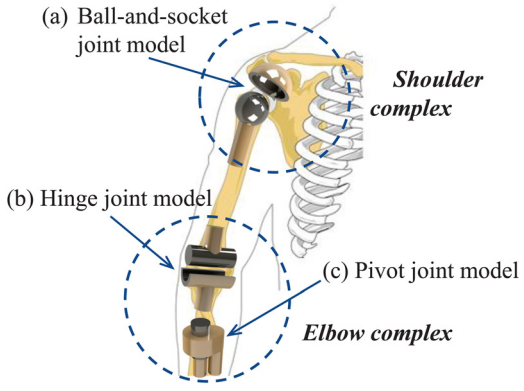

Fig. 4 Mechanical models of the upper limb joints: (*a*) ball-and-socket joint model, (*b*) hinge joint model, and (*c*) pivot joint model

Downloaded From: http://dynamicsystems.asmedigitalcollection.asme.org/ on 05/14/2018 Terms of Use: http://www.asme.org/about-asme/terms-of-use

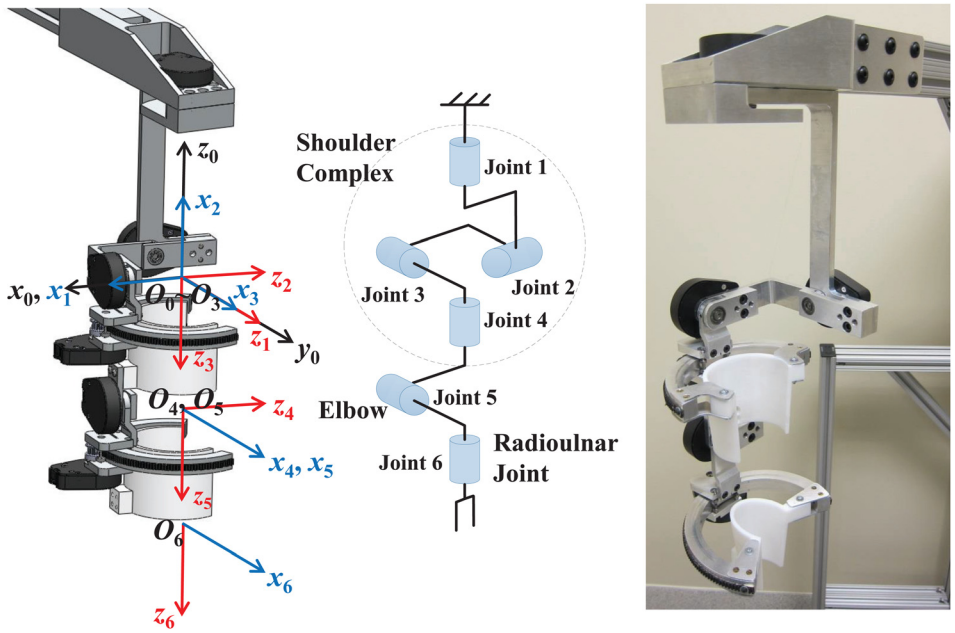

Fig. 5 Left: computer-aided design (CAD) model with coordinate frames in exoskeleton home posture. Middle: simplified joint model. Right: physical hardware design implementation.

elbow joint and the radioulnar joint are each modeled by one single DOF.

Exoskeletons are supposed to be wearable, and thus, the prosthetic joints of an upper limb exoskeleton can be classified into two types: one with rotation axis being perpendicular to the arm segments (joints 1, 2, 3, and 5, Fig. 6(*a*)) and the other one with rotation axis being along the longitude of the arm segments (joints 4 and 6, Fig. 6(*b*)). Two cuffs 3D-printed following macaque arm morphology with elastic braces are used to attach the exoskeleton to the macaque arm, and an opening is left for each cuff for easy attachment as well as avoiding collision between the exoskeleton cuff and macaque body. A curved guide rail, a sliding roller with bearing groups, and a timing belt with pulley are mounted on the cuff to transmit the rotation motion of the upper arm and the forearm to the sensors.

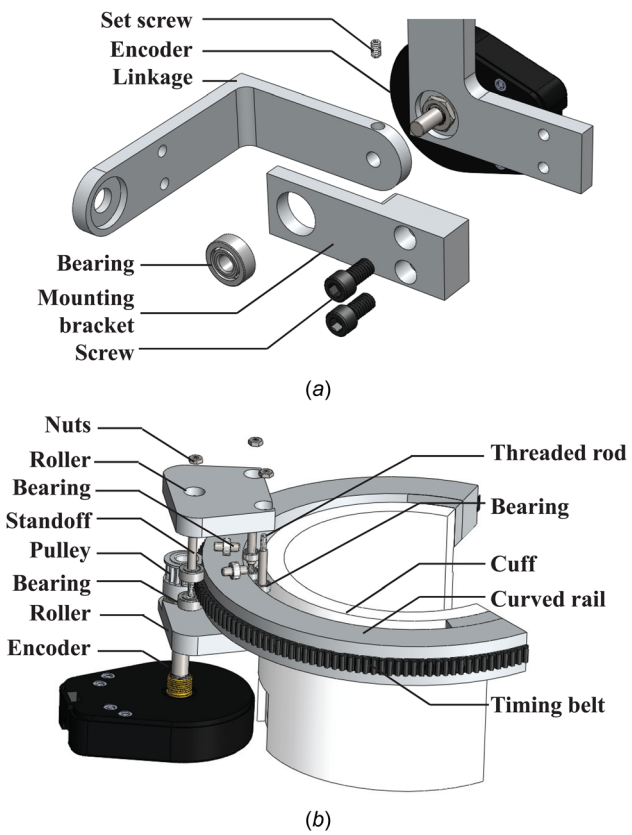

Fig. 6 CAD design of two types of joints: (*a*) joint type I and (*b*) joint type II

Compared with human ADL ROM, most designed mechanical joint limits (listed in the last column of Table 2) meet the design requirements. The designed ROM of the elbow joint is restricted by the spacial limitations due to the mechanical collision between forearm and upper arm cuffs, but since the interested BMI task is prescribed as always in front of the macaque's coronal plane and generally does not involve elbow flexion of over 90 deg, the designed ROMs of each joint satisfy the specified requirements.

2.4 Real-Time Motion Data Acquisition. For real-time motion data acquisition, a target PC consisting of an NI FPGA board (NI 7851R) running real-time and FPGA modules is used for collecting the measurements of the encoders, and a host PC serves as a terminal for monitoring and analyzing the data acquisition process, as shown in Fig. 3.

3 Kinematic Modeling and Analysis

To evaluate the effectiveness of the proposed shoulder joint model to avoid kinematic singularities in future actuated exoskeleton designs, the kinematic properties of the proposed 4DOF shoulder model will be investigated in this section.

3.1 System Kinematic Model. Denavit–Hartenberg (DH) parameters can fully define the kinematic model of a mechanism. Let $\boldsymbol{\theta} \in \mathbb{R}^6$ be the joint variable, then the DH parameters of the proposed exoskeleton model are as shown in Table 3 following the frame definition in Fig. 5, where L_1 and L_2 are the distance from the shoulder center to the elbow and the distance from the elbow to the palm, respectively. The posture at $\boldsymbol{\theta} = [\pi/4, -\pi/2, \pi/2, 0, 0, 0]^\top$ is defined as the *home posture* of the exoskeleton.

Downloaded From: http://dynamicsystems.asmedigitalcollection.asme.org/ on 05/14/2018 Terms of Use: http://www.asme.org/about-asme/terms-of-use

Table 3 DH parameters of the proposed upper limb exoskeleton

Joint	θ (deg)	d	a	α (deg)
1	$-50.5 \le \theta_1 \le 140.5$	0	0	−90
2	$-228.3 \le \theta_2 \le 48.3$	0	0	90
3	$-98.1 \le \theta_3 \le 98.1$	0	0	−90
4	$-80 \le \theta_4 \le 80$	L_1	0	90
5	$-88.7 \le \theta_5 \le 8.1$	0	0	−90
6	$-80 \le \theta_6 \le 80$	L_2	0	0

3.2 Singularity and Manipulability of Shoulder Joint. The Jacobian matrix loses rank at singularities. For the ball-and-socket shoulder joint model with fixed upper arm length, the end point moves on a spherical surface. Thus, the orientation Jacobian $\boldsymbol{J}_o(\boldsymbol{\theta})$ which maps the angular velocities of the first four joints to the elbow's task space angular velocities is derived as

$$\boldsymbol{J}_o(\boldsymbol{\theta}) = \begin{bmatrix} 0 & -s_1 & c_1 s_2 & -c_1 c_2 s_3 - s_1 c_3 \\ 0 & c_1 & s_1 s_2 & -s_1 c_2 s_3 + c_1 c_3 \\ 1 & 0 & c_2 & s_2 s_3 \end{bmatrix} \tag{1}$$

where $s_i = \sin(\theta_i)$ and $c_i = \cos(\theta_i)$. $\boldsymbol{J}_o(\boldsymbol{\theta})$ becomes rank deficient at $(\theta_2, \theta_3) = (-\pi, 0)$, the only singularity in the workspace of the proposed shoulder model, as shown in Fig. 7 where axis 1 is collinear with axis 3 and axis 2 is collinear with axis 4. However, the possibility of the device entering the shoulder joint's singularity is extremely low. This is because that the singular configuration corresponds to the motion sequence of a 90 deg shoulder abduction followed by a 90 deg shoulder horizontal rotation from the home position as shown in Fig. 8. It can be noticed that when only axis 3 is rotated to achieve the 90 deg horizontal rotation motion, the shoulder joint will be singular; but if the motion is realized by a nonzero rotation of axis 1, singularity will not occur. For a passive device, the chances of almost zero axis 1 motion during such a 90 deg horizontal rotation are low. Besides, the designed animal training tasks rarely involve motion of this kind, which will be detailed in Sec. 5.

To quantitatively evaluate the mechanism's manipulation ability, the measure of *manipulability* [21] can be defined as

$$c_m(\boldsymbol{\theta}) = \sqrt{\det\left(\boldsymbol{J}(\boldsymbol{\theta})\boldsymbol{J}(\boldsymbol{\theta})^\top\right)} \tag{2}$$

where $\boldsymbol{J}(\boldsymbol{\theta})$ is a general Jacobian matrix.

The manipulability of a mechanism depends on its link lengths, number of joints, and the dimension of its task space. In order to compare manipulabilities of different manipulators working in different workspaces, Kim and Khosla [22] proposed the concept *relative manipulability* which is independent of scales and dimension orders

$$c_{\text{rel}}(\boldsymbol{\theta}) = \frac{\sqrt[m]{\det\left(\boldsymbol{J}(\boldsymbol{\theta})\boldsymbol{J}(\boldsymbol{\theta})^\top\right)}}{\sqrt{\sum_{i=1}^{n}\left(a_i^2 + d_i^2\right)}} \tag{3}$$

where n is the number of joints, m is the dimension order of the task space, and a_i and d_i are the ith link length and joint offset defined in the DH parameters convention, respectively.

The manipulability or relative manipulability provides a measure of the dexterity of the exoskeleton given a joint space configuration. The mapping from the joint space to the task space may not be unique, in particular, for redundant mechanisms or scenarios where only partial task space constraints are considered (e.g., positions without orientations). Then, the manipulability of a particular task space point may take multiple values. Thus, we introduce the terminology *manipulability distribution* here. As an example to demonstrate the advantage of the proposed design, the manipulability distributions of the rotational DOF on the task space transverse plane (i.e., the $x_0O_0y_0$ plane defined in Fig. 5) are investigated for the following four models: the conventional standard triad model (IKO [23]), the triad models with rarely reached singular direction ((CADEN)-7), and with optimized axis relative angles (MEDARM), as well as the proposed model. The performance of the exoskeleton on this horizontal plane is important considering the designed BMI tasks previously discussed. An illustration of the manipulability study is shown in Fig. 9 with the elbow position as the investigated endpoint.

Figure 10 plots the manipulability distributions of the four models with their end points at different directions ($\beta = -50$ deg to 140 deg, defined in Fig. 9) on the horizontal plane. Figure 10(*a*) shows the manipulability distribution of the IKO shoulder joint model. It uses rotation convention (*a*) of Fig. 2 with the strict forward direction ($\beta = 90$ deg) as its singular direction on the horizontal plane. Each posture is uniquely determined by one joint space realization due to its possession of only 3DOFs, which means the singularity will always occur (i.e., the manipulability vanishes) in the vicinity of the strict forward direction, and one rotational DOF (either shoulder flexion/extension or abduction/adduction) will be lost.

Figure 10(*b*) presents the manipulability distribution of the shoulder joint of (CADEN)-7. This design is also an orthogonal triad model using the rotation convention (*a*) of Fig. 2. But with the first joint axis having an acute angle about the vertical direction, the singularity of this model was designed in a direction that is rarely (statistically) reached by the subject. Thus, compared with the IKO shoulder joint model, there are no "hard" singularities within the feasible workspace (in the horizontal plane), and the average manipulability is improved. However, singularities still exist in some other regions of the workspace (outside the horizontal plane). Therefore, it is still possible for the subject to enter the vicinity of the singular region, resulting in limited feasible workspace.

Figure 10(*c*) plots the manipulability distribution of the MEDARM shoulder joint. It features the first two revolute axes with an optimized angle rather than an orthogonal relationship. By inclusion of an "azimuth" (not a full azimuth) axis, the ROM on the horizontal plane is extended, though some regions are physically unable to be reached by a macaque. Besides, the nonunique inverse kinematic solutions lead to multiple joint space realizations since only task space positions (not orientations) are considered in this example. Thus, it has more flexibility regarding the upper arm's motion on the horizontal plane. However, its average manipulability is relatively low due to its lack of a dedicated internal/external rotation joint for the upper arm.

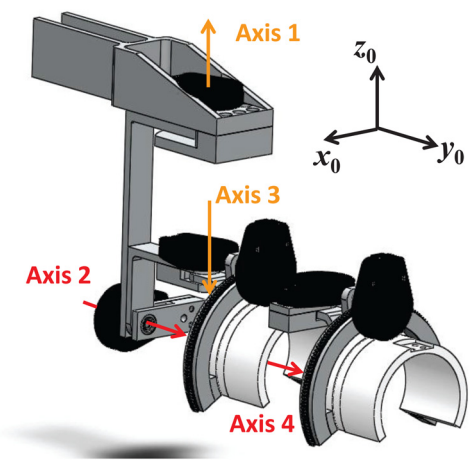

Fig. 7 Singular posture of the proposed 4DOF shoulder complex model

Downloaded From: http://dynamicsystems.asmedigitalcollection.asme.org/ on 05/14/2018 Terms of Use: http://www.asme.org/about-asme/terms-of-use

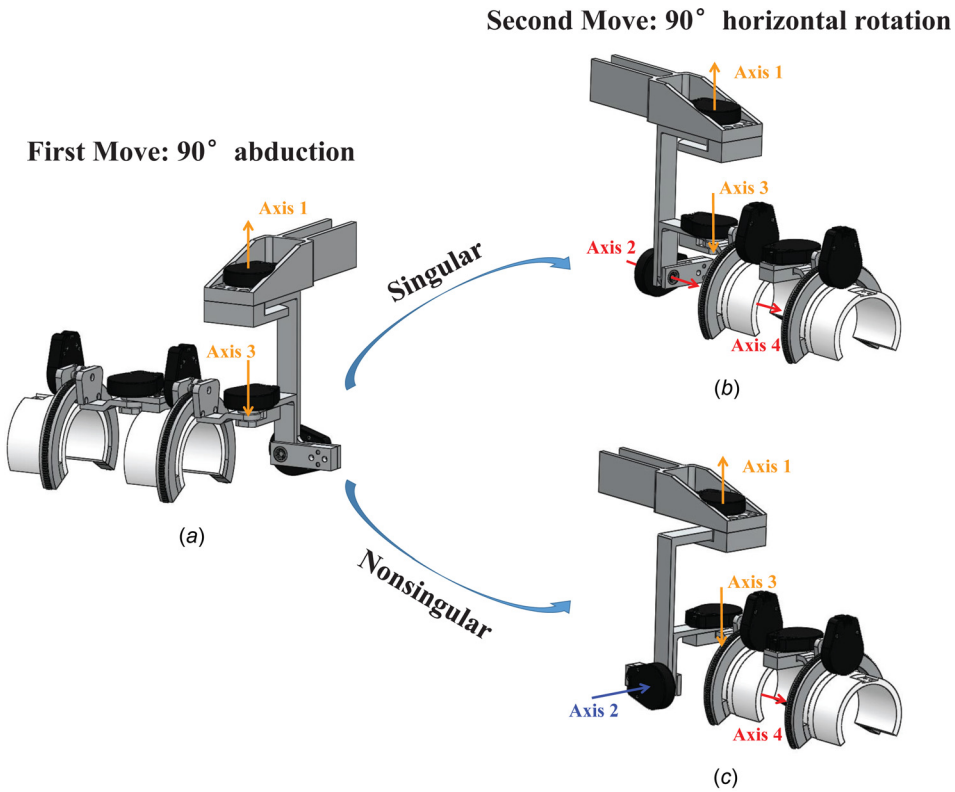

Fig. 8 Illustration of a motion sequence leading to the singular shoulder joint configuration

Figure 10(*d*) shows the manipulability distribution of our proposed model with 4DOFs combining both of the two glenohumeral joint rotation conventions (Figs. 2(*a*) and 2(*b*)). From Figs. 10(*a*)–10(*d*), the improvement of the manipulabilities is evident. With an azimuth axis, this model enjoys the similar multiple joint space realizations as the MEDARM model on the horizontal plane. The inclusion of a standard triad model following the azimuthal DOF makes it possible to obtain the maximal manipulability value in all directions (i.e., the feasible workspace is the whole horizontal plane). In fact, each posture of the proposed shoulder joint model possesses different levels of manipulabilities. Thus, it is possible for an actuated mechanism with the same kinematic structure to avoid the singular configuration by properly selecting the joint space trajectories, and one typical approach is the gradient projection control [24]. Similar manipulability advantages can also be found in other regions of the workspace.

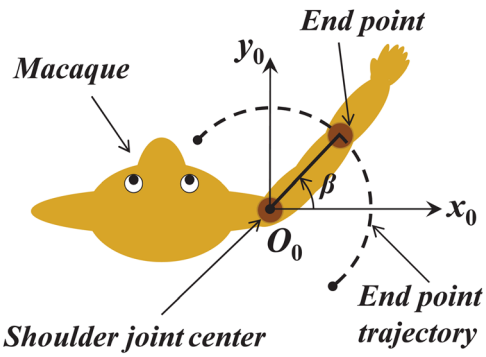

Fig. 9 Top view of macaque on the transverse plane. Macaque is plotted with its shoulder joint center fixed and its elbow as the end point.

4 System Kinematic Calibration

Encoders are mounted on the proposed passive exoskeleton as the position sensors. Here, the U.S. Digital S6 incremental optical encoders are selected with 2500 counts per round for each joint, and encoder indices are utilized to indicate the reference positions.

For the current setup, position measurement error comes from two major sources—the unknown encoder value offsets at exoskeleton home posture and the kinematic model uncertainties. Kinematic calibration needs to be conducted to reduce the position measurement error. An external optical tracking system is a nice candidate for providing 3D position information as the reference values. By comparing the position data in the tracking system frame and the exoskeleton frame, the unknown variable values can be identified using an optimization-based approach. Note that this is an offline process, which only needs to be completed once before the exoskeleton is put into use.

4.1 Calibration Setup. Our optical tracking setup is the PhaseSpace IMPULSE X2 Motion Capture System consisting of ten cameras with a sampling rate of 480 Hz. This system can track its active light-emitting diode markers and has submillimeter accuracy [25]. To acquire the position information of the exoskeleton, one marker was rigidly attached to the endpoint of the last link (Fig. 11). The endpoint was moved along some arbitrary trajectory in the task space during which all six joints were involved as much as possible. The positions of the marker were recorded by the motion capture system, and the joint space motions by each encoder. The sampling rate of the encoder reading is 1 kHz, and the two data acquisition systems were synchronized via the Network Time Protocol.

Downloaded From: http://dynamicsystems.asmedigitalcollection.asme.org/ on 05/14/2018 Terms of Use: http://www.asme.org/about-asme/terms-of-use

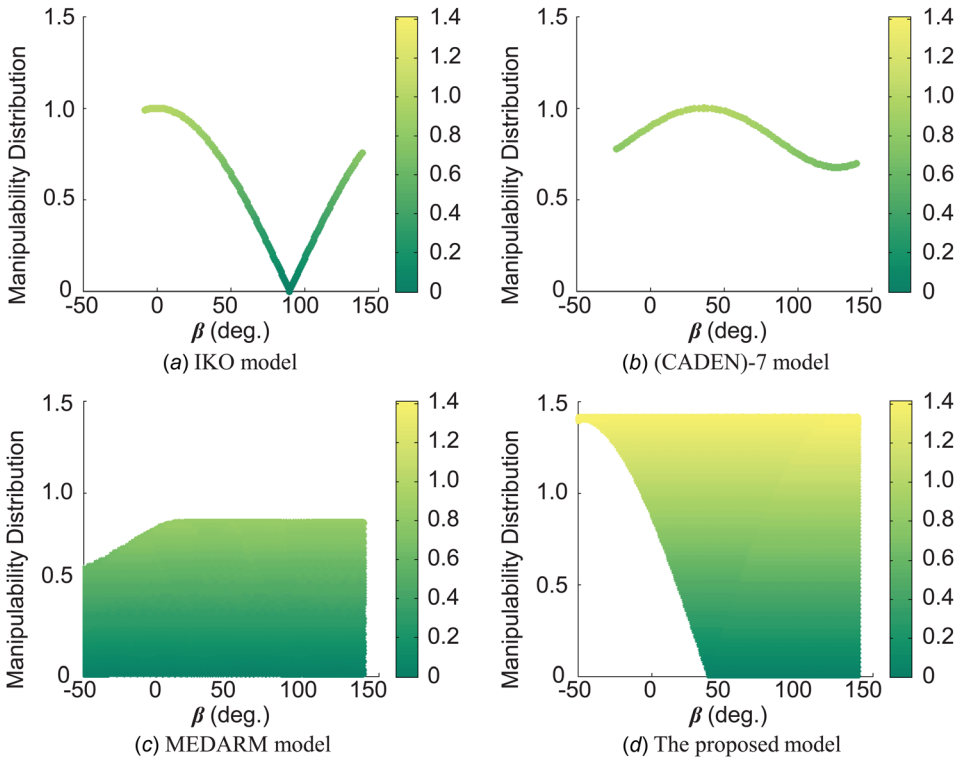

Fig. 10 Manipulability distributions of four models on the horizontal plane: (*a*) IKO model, (*b*) (CADEN)-7 model, (*c*) MEDARM model, and (*d*) the proposed model

4.2 Calibration Algorithm. Calibration algorithm for the jth sampling point is shown in Fig. 12 (variables in red are to be identified). Define $\Delta\boldsymbol{\theta}^0 \in \mathbb{R}^6$ as the vector of all six encoder offsets at exoskeleton's home posture. Together with the encoder readings $\boldsymbol{\theta}^{R,j}$, the joint space variable $\boldsymbol{\theta}^j$ can be expressed as

$$\boldsymbol{\theta}^j = \Delta\boldsymbol{\theta}^0 + \boldsymbol{\theta}^{R,j} \tag{4}$$

Introduce $\Delta\boldsymbol{p}^M \in \mathbb{R}^3$ as the marker's coordinates deviation from its nominal and actual value in the O_6–$x_6y_6z_6$ frame (following the definition in Fig. 5). Then, the marker position in the exoskeleton's frame $\boldsymbol{p}^j_{\text{exo}}$ can be obtained via the coordinate transformation matrix $\boldsymbol{T}^0_6(\Delta\boldsymbol{\zeta}, \boldsymbol{\theta}^j)$ by forward kinematics, where $\Delta\boldsymbol{\zeta} := [\Delta d_2, \Delta d_3, \Delta d_5, \Delta a_3, \Delta a_5]^\top \in \mathbb{R}^5$ represents the vector of the concerned deviations of the exoskeleton nominal DH parameters from their actual values. Besides, as shown in Fig. 11, the relative posture between the camera frame and the exoskeleton frame is not exactly known, and thus, two additional variables $\boldsymbol{d} \in \mathbb{R}^3$ and $\boldsymbol{\varphi} \in \mathbb{R}^3$ are introduced to represent the relative translations and rotations (Euler angles) between the two frames, respectively. The marker's coordinates in the camera frame $\boldsymbol{p}^j_{\text{cam}}(\Delta\boldsymbol{\theta}^0, \Delta\boldsymbol{\zeta}, \Delta\boldsymbol{p}^M, \boldsymbol{d}, \boldsymbol{\varphi})$ can be calculated through the frame transformation matrix $\boldsymbol{A}^{\text{cam}}_{\text{exo}}(\boldsymbol{d}, \boldsymbol{\varphi})$ with knowledge of the encoder information. On the other hand, the marker's coordinates in the camera frame $(\boldsymbol{p}^j_{\text{cam}})^*$ can be directly acquired by the cameras, which serve as the reference in this calibration process. Thus, the position error is

$$e^j = ||(\boldsymbol{p}^j_{\text{cam}})^* - \boldsymbol{p}^j_{\text{cam}}(\Delta\boldsymbol{\theta}^0, \Delta\boldsymbol{\zeta}, \Delta\boldsymbol{p}^M, \boldsymbol{d}, \boldsymbol{\varphi})||_2 \tag{5}$$

Select N calibration points along the trajectory, and define $\boldsymbol{x} := \left[(\Delta\boldsymbol{\theta}^0)^\top, (\Delta\boldsymbol{\zeta})^\top, (\Delta\boldsymbol{p}^M)^\top, \boldsymbol{d}^\top, \boldsymbol{\varphi}^\top\right]^\top$ as the parameter vector to be identified. Then, the calibration algorithm can be cast as the following optimization problem:

$$\begin{aligned} \min_{\boldsymbol{x}} \quad & \sum_{j=1}^{N} \|(\boldsymbol{p}^j_{\text{cam}})^* - \boldsymbol{p}^j_{\text{cam}}(\boldsymbol{x})\|_2^2 \\ \text{s.t.} \quad & x_i^L \le x_i \le x_i^U, \quad i = 1, 2, \ldots, 20 \end{aligned} \tag{6}$$

where x_i^L is the lower bound of the corresponding element and x_i^U is the upper bound. This is a typical nonlinear least squares problem and can be solved using the lsqnonlin command in the MATLAB Optimization Toolbox [26].

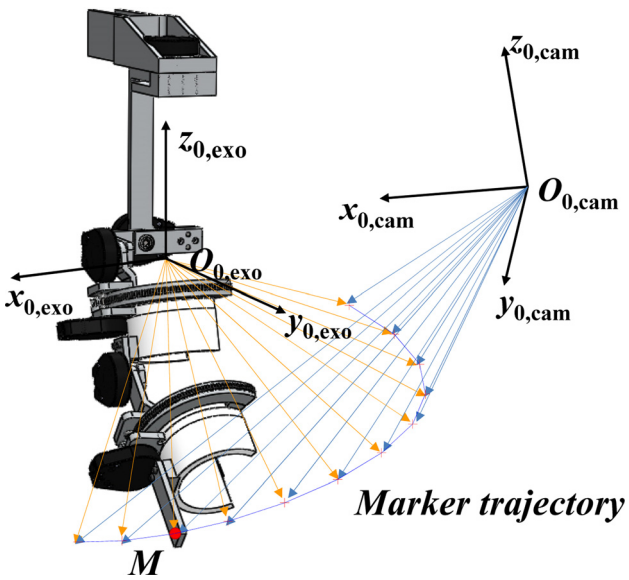

Fig. 11 Illustration of synchronized data acquisition of the exoskeleton system and the motion capture system

Downloaded From: http://dynamicsystems.asmedigitalcollection.asme.org/ on 05/14/2018 Terms of Use: http://www.asme.org/about-asme/terms-of-use

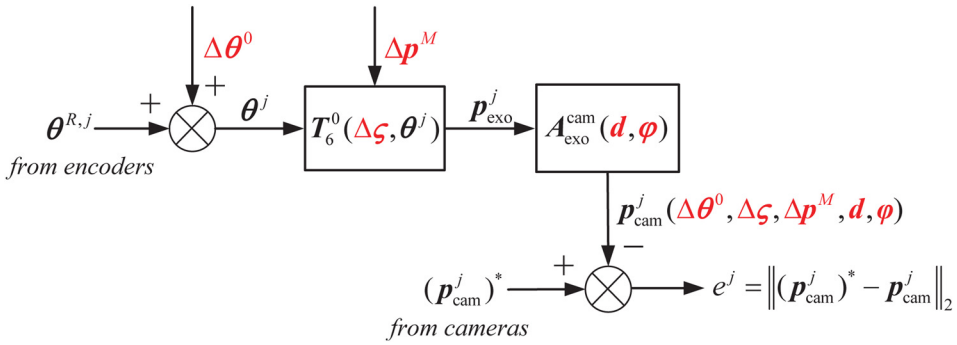

Fig. 12 Block diagram of the calibration algorithm

4.3 Experiment Results and Analysis

4.3.1 Parameter Identification. A total of 400 data points are sampled in one experiment session for parameter training. Figure 13 shows the comparison between data fitting results before and after calibration with the blue lines representing the position errors. The identification results and initial guesses (nominal mechanical design values for system dimensions and manually tested values for encoder offsets) are listed in Table 4. Before kinematic calibration, the root-mean-square (RMS) position error of the training dataset was 13.6 mm with the mean of 13.6 mm and standard deviation of 1.35 mm; and after kinematic calibration, the RMS position error of the same training dataset became 1.05 mm with the mean of 0.95 mm and standard deviation of 0.44 mm, which demonstrates the effectiveness of the proposed kinematic calibration approach.

Table 4 Experimental results of the proposed approach

Para.	Guess	Results	Para.	Guess	Results
$\Delta\theta_1^0$ (deg)	30.7	31.85	Δa_5 (mm)	0	0.03
$\Delta\theta_2^0$ (deg)	−16.3	−17.60	Δp_x^M (mm)	0	−0.10
$\Delta\theta_3^0$ (deg)	−15.2	−13.45	Δp_y^M (mm)	0	−0.16
$\Delta\theta_4^0$ (deg)	−17.1	−17.19	Δp_z^M (mm)	0	−8.46
$\Delta\theta_5^0$ (deg)	−25.5	−22.11	d_x (mm)	203.2	203.29
$\Delta\theta_6^0$ (deg)	−2.3	−2.39	d_y (mm)	852.1	849.31
Δd_2 (mm)	0	−1.79	d_z (mm)	216.8	224.30
Δd_3 (mm)	0	−0.48	φ_x (deg)	−90.0	−89.01
Δd_5 (mm)	0	2.80	φ_y (deg)	0	−0.10
Δa_3 (mm)	0	−4.01	φ_z (deg)	−135.0	−135.52

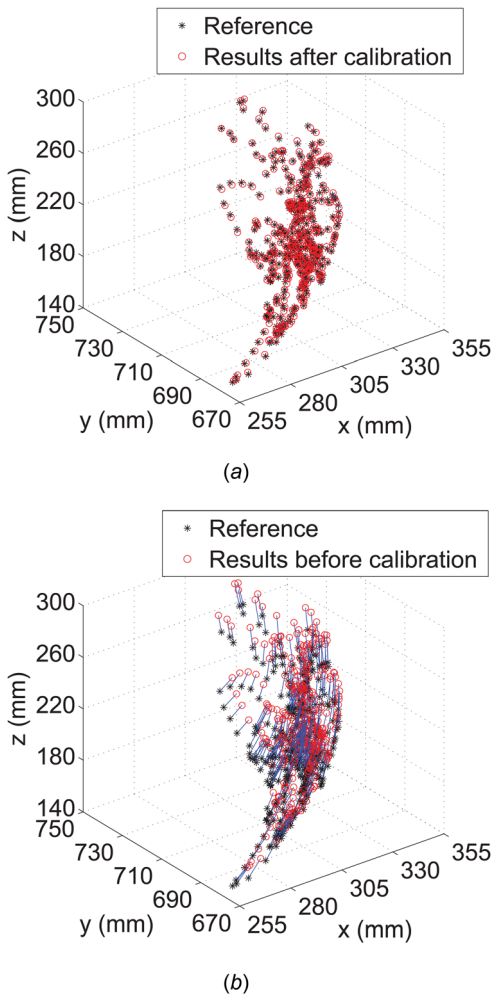

Fig. 13 Sampled marker positions in the camera frame for reference data and generated data (*a*) before and (*b*) after calibration

4.3.2 Cross-Validation. To evaluate the results, cross-validations were conducted using six datasets of 300 data points downsampled from other experimental sessions. Position errors of the cross-validation and the training datasets are given in Fig. 14. It can be noticed that the position errors of the cross-validation datasets are approximately the same level as the training dataset. Considering the accuracy levels of state-of-the-art neural decoders with virtual cursors [27,28], the positioning accuracy of this exoskeleton is within acceptable levels.

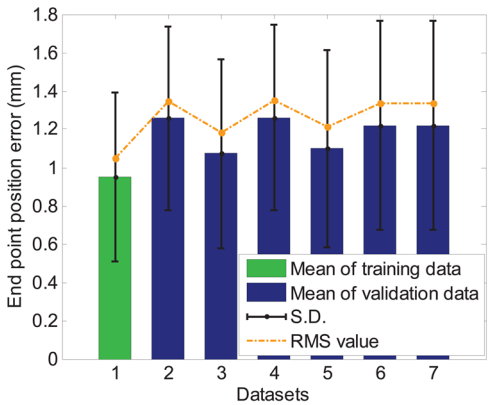

Fig. 14 Position errors of both training and cross-validation datasets

Downloaded From: http://dynamicsystems.asmedigitalcollection.asme.org/ on 05/14/2018 Terms of Use: http://www.asme.org/about-asme/terms-of-use

Fig. 15 Experiment scene of a macaque wearing the proposed exoskeleton

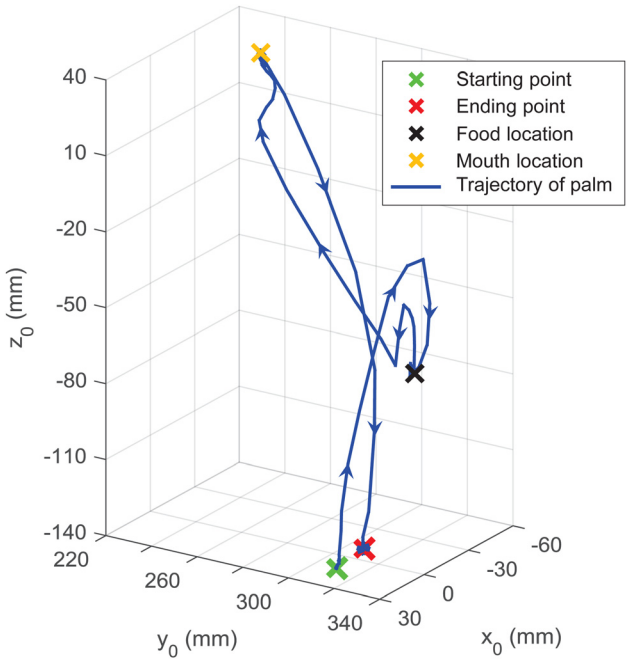

Fig. 17 Task space trajectory of the macaque palm for one trial. The palm was initially placed on the primate table, and the macaque started to reach the food, grasped, and fed itself when some food was placed in front of it, and finally placed its palm back on the table. The coordinate system O_0–$x_0y_0z_0$ follows the convention in Fig. 5, and the macaque sat facing the positive direction of the y_0 axis.

5 Animal Test Results

In order to verify the effectiveness of the proposed exoskeleton system, animal tests of a self-feeding task were performed with one adult male rhesus macaque. All procedures were conducted in compliance with the National Institute of Health Guide for Care and Use of Laboratory Animals and were approved by the University of California, Berkeley Institutional Animal Care and Use Committee. Figure 15 shows the experiment scene of an able-bodied macaque wearing the proposed exoskeleton. Some food was presented in front of the macaque, and the macaque voluntarily performed the reaching, grasping, and finally self-feeding motion. The linkages of the exoskeleton were made of thin aluminum bars and the cuffs were 3D-printed using acrylonitrile butadiene styrene. Thus, it is considered that the entire passive exoskeleton is light enough for the macaque to operate, which can be observed during the animal's self-feeding motion. Besides, a compression spring was used to connect the second linkage and the beam of the exoskeleton frame to help the exoskeleton maintain in its home position (gravity compensation) when no subject was attached.

A total of 25 trials were performed within 7 mins. Figure 16 plots the joint space trajectories of all six joints for one trial, and a 3D task space trajectory of the macaque palm is presented in Fig. 17 for more intuitive visualization by performing the forward kinematics to the joint space motion measurements (assuming rigid wrist joint), which matched the actual motion well and supported the effectiveness of the proposed exoskeleton system.

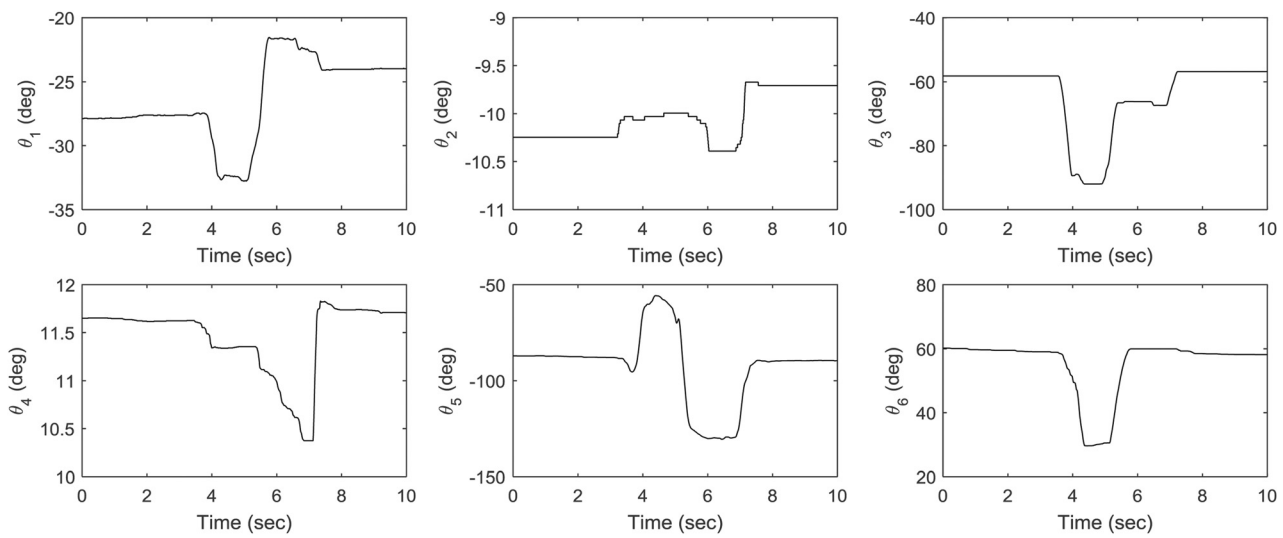

Fig. 16 Joint space trajectory of the reach–grasp–feed task for one trial

Downloaded From: http://dynamicsystems.asmedigitalcollection.asme.org/ on 05/14/2018 Terms of Use: http://www.asme.org/about-asme/terms-of-use

Table 5 Measured macaque ROM in reach–grasp–feed task

Joint	Motion	ROM (deg)	Joint	Motion	ROM (deg)
1	Azi. add./abd.	30.9	4	Shld. int./ext.	39.9
2	Shld. add./abd.	5.1	5	Elbw. int./ext	84.7
3	Shld. flx./ext.	75.3	6	Pron./supi.	54.9

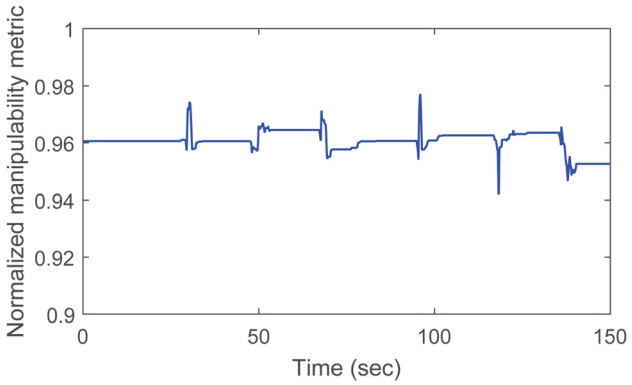

Fig. 18 Normalized manipulability metric of the shoulder joint for six trials within 150 s

Table 5 lists the measured ROMs of all 6DOFs during the 25 trials, which indicates that the ROM of each joint provided by the exoskeleton (see Table 2) is sufficient for the designed task. Figure 18 shows the time series of the normalized manipulability metric of the shoulder joint for six trials within 150 s. Notice that the normalized manipulability metric remained at a high level, which demonstrates the manipulation flexibility of the proposed shoulder joint during the animal training tasks.

6 Conclusions

This paper presents a 6DOF passive upper limb exoskeleton for macaque monkeys. Four DOFs were assigned at the shoulder joint to achieve more flexible manipulation of the mechanism.

The kinematic singularity of the proposed shoulder complex model was discussed and quantitatively investigated based on the manipulability metric. The manipulabilities of four different shoulder complex designs were compared, and the results indicated that the proposed model had the ability to avoid entering the vicinity of system singularity by appropriately planning joint space trajectories.

Real-time data acquisition of the exoskeleton system was set up, and approximately 2 mm end point position sensing accuracy was achieved by kinematic calibration, which is sufficient for the neurophysiology applications. Animal tests were conducted in the scenario of a reach–grasp–feed task. Both task space trajectory visualization and measured ROM of each joint demonstrate the effectiveness of the proposed exoskeleton system.

The motion sensing functionality of the proposed exoskeleton helps analyze the motion characteristics in the sense of each individual joint of the upper limb, which will provide guidance for our future motorized macaque exoskeleton designs.

Acknowledgment

This work was supported by the National Science Foundation under Grant No. EFRI-M3C 1137267. We would like to thank Dr. Joonbum Bae and Dr. Simon Overduin for their earlier effort on this project. We also want to thank Dr. Gregorij Kurillo and Robert Matthew for their help in system calibration, and Dennis Lee and Mick Franssen for their assistance in the hardware fabrication.

References

[1] Carmena, J. M., 2013, "Advances in Neuroprosthetic Learning and Control," PLoS Biol., **11**(5), p. e1001561.
[2] Velliste, M., Perel, S., Spalding, M. C., Whitford, A. S., and Schwartz, A. B., 2008, "Cortical Control of a Prosthetic Arm for Self-Feeding," Nature, **453**(7198), pp. 1098–1101.
[3] Hochberg, L. R., Bacher, D., Jarosiewicz, B., Masse, N. Y., Simeral, J. D., Vogel, J., Haddadin, S., Liu, J., Cash, S. S., van der Smagt, P., and Donoghue, J. P., 2012, "Reach and Grasp by People With Tetraplegia Using a Neurally Controlled Robotic Arm," Nature, **485**(7398), pp. 372–375.
[4] Nef, T., and Riener, R., 2008, "Shoulder Actuation Mechanisms for Arm Rehabilitation Exoskeletons," 2nd IEEE RAS and EMBS International Conference on Biomedical Robotics and Biomechatronics, Scottsdale, AZ, Oct. 19–22, pp. 862–868.
[5] Scott, S. H., 1999, "Apparatus for Measuring and Perturbing Shoulder and Elbow Joint Positions and Torques During Reaching," J. Neurosci. Methods, **89**(2), pp. 119–127.
[6] Gopura, R. A. R. C., and Kiguchi, K., 2009, "Mechanical Designs of Active Upper-Limb Exoskeleton Robots: State-of-the-Art and Design Difficulties," IEEE International Conference on Rehabilitation Robotics (ICORR), Kyoto, Japan, June 23–26, pp. 178–187.
[7] Medical Multimedia Group, 2008, "Orthopedic Information," Medical Multimedia Group, LLC, Missoula, MT.
[8] Wu, G., van der Helm, F. C. T., Veeger, H. E. J., Makhsous, M., van Roy, P., Anglin, C., Nagels, J., Karduna, A. R., McQuade, K., Wang, X., Werner, F. W., and Buchholz, B., 2005, "ISB Recommendation on Definitions of Joint Coordinate Systems of Various Joints for the Reporting of Human Joint Motion—Part II: Shoulder, Elbow, Wrist and Hand," J. Biomech., **38**(5), pp. 981–992.
[9] Ball, S., Brown, I., and Scott, S., 2007, "MEDARM: A Rehabilitation Robot With 5DOF at the Shoulder Complex," IEEE/ASME International Conference on Advanced Intelligent Mechatronics (AIM), Zurich, Switzerland, Sept. 4–7.
[10] Ergin, M. A., and Patoglu, V., 2012, "ASSISTON-SE: A Self-Aligning Shoulder-Elbow Exoskeleton," IEEE International Conference on Robotics and Automation (ICRA), Saint Paul, MN, May 14–18, pp. 2479–2485.
[11] Romilly, D. P., Anglin, C., Gosine, R. G., Hershler, C., and Raschke, S. U., 1994, "A Functional Task Analysis and Motion Simulation for the Development of a Powered Upper-Limb Orthosis," IEEE Trans. Rehabil. Eng., **2**(3), pp. 119–129.
[12] Perry, J., Rosen, J., and Burns, S., 2007, "Upper-Limb Powered Exoskeleton Design," IEEE/ASME Trans. Mechatronics, **12**(4), pp. 408–417.
[13] Letier, P., Avraam, M., Veillerette, S., Horodinca, M., Bartolomei, M. D., Schiele, A., and Preumont, A., 2008, "SAM: A 7-DOF Portable Arm Exoskeleton With Local Joint Control," IEEE/RSJ International Conference on Intelligent Robots and Systems (IROS), Nice, France, Sep. 22–26, pp. 3501–3506.
[14] Cheng, E. J., and Scott, S. H., 2000, "Morphometry of *Macaca mulatta* Forelimb. I. Shoulder and Elbow Muscles and Segment Inertial Parameters," J. Morphol., **245**(3), pp. 206–224.
[15] Huston, R., 2009, *Principles of Biomechanics*, Taylor & Francis CRC Press, Boca Raton, FL.
[16] Schell, K., Bradley, E., Bucher, L., Seckel, M., Lyons, D., Wakai, S., Bartell, D., Carson, E., Chichester, M., Foraker, T., and Simpson, K., 2006, "Clinical Comparison of Automatic, Noninvasive Measurements of Blood Pressure in the Forearm and Upper Arm," Am. J. Crit. Care, **15**(2), pp. 196–205.
[17] Cott, H. P. V., and Kinkade, R. G., 1972, *Human Engineering Guide to Equipment Design*, Revised ed., McGraw-Hill, Washington, DC.
[18] Christel, M. I., and Billard, A., 2002, "Comparison Between Macaques' and Humans' Kinematics of Prehension: The Role of Morphological Differences and Control Mechanisms," Behav. Brain Res., **131**(1–2), pp. 169–184.
[19] Chan, S. S., and Moran, D. W., 2006, "Computational Model of a Primate Arm: From Hand Position to Joint Angles, Joint Torques and Muscle Forces," J. Neural Eng., **3**(4), pp. 327–337.
[20] Yang, J., Abdel-Malek, K., and Nebel, K., 2005, "Reach Envelope of a 9-Degree-of-Freedom Model of the Upper Extremity," Int. J. Rob. Autom., **20**(4), pp. 240–259.
[21] Yoshikawa, T., 1985, "Manipulability of Robotic Mechanisms," Int. J. Rob. Res., **4**(2), pp. 3–9.
[22] Kim, J.-O., and Khosla, P. K., 1991, "Dexterity Measures for Design and Control of Manipulators," IEEE/RSJ International Workshop on Intelligent Robots and Systems (IROS), Osaka, Japan, Nov. 3–5, Vol. 2, pp. 758–763.
[23] Martinez, F., Retolaza, I., Pujana-Arrese, A., Cenitagoya, A., Basurko, J., and Landaluze, J., 2008, "Design of a Five Actuated DoF Upper Limb Exoskeleton Oriented to Workplace Help," 2nd IEEE RAS and EMBS International Conference on Biomedical Robotics and Biomechatronics (BioRob), Scottsdale, AZ, Oct. 19–22, pp. 169–174.
[24] Siciliano, B., Sciavicco, L., Villani, L., and Oriolo, G., 2009, *Robotics: Modelling, Planning and Control*, 2nd ed., Springer, London.
[25] PhaseSpace, 2012, "The IMPULSE X2 Motion Capture System Catalog," PhaseSpace, Inc., San Leandro, CA.
[26] MathWorks, 2012, "Optimization Toolbox," MathWorks, Inc., Natick, MA.
[27] Gilja, V., Nuyujukian, P., Chestek, C. A., Cunningham, J. P., Yu, B. M., Fan, J. M., Churchland, M. M., Kaufman, M. T., Kao, J. C., Ryu, S. I., and Shenoy, K. V., 2012, "A High-Performance Neural Prosthesis Enabled by Control Algorithm Design," Nat. Neurosci., **15**(12), pp. 1752–1757.
[28] Shanechi, M. M., Orsborn, A. L., and Carmena, J. M., 2016, "Robust Brain-Machine Interface Design Using Optimal Feedback Control Modeling and Adaptive Point Process Filtering," PLoS Comput. Biol., **12**(4), p. e1004730.

Downloaded From: http://dynamicsystems.asmedigitalcollection.asme.org/ on 05/14/2018 Terms of Use: http://www.asme.org/about-asme/terms-of-use